IEEE Access
Multidisciplinary | Rapid Review | Open Access Journal

Received July 17, 2021, accepted August 6, 2021, date of publication August 9, 2021, date of current version August 16, 2021.

Digital Object Identifier 10.1109/ACCESS.2021.3103813

Assessment of mmWave Exposure From Antenna Based on Transformation of Spherical Wave Expansion to Plane Wave Expansion

YINLIANG DIAO[1], (Member, IEEE), AND AKIMASA HIRATA[1,2], (Fellow, IEEE)
[1]Department of Electrical and Mechanical Engineering, Nagoya Institute of Technology, Nagoya 466-8555, Japan
[2]Center of Biomedical Physics and Information Technology, Nagoya Institute of Technology, Nagoya 466-8555, Japan

Corresponding author: Akimasa Hirata (ahirata@nitech.ac.jp)

This work was supported by the Ministry of Internal Affairs and Communications, Japan, under Grant JPMI10001.

ABSTRACT To protect human beings from overexposure to mmWave electromagnetic fields, international guidelines and standard specified the (exposure) reference level in terms of the peak spatial-average incident power density (*ps*PD). In this study, we proposed a method to effectively assess the *ps*PD from a mmWave antenna using its spherical near-field measurement data. This method employed the transformation of spherical wave expansion to plane wave expansion to reconstruct the electric and magnetic field components on an evaluation plane in front of the antenna aperture. The *ps*PD was subsequently obtained based on the time-average Poynting vector. The accuracy of the proposed method was validated by comparing it with full-wave simulation results using 12 array antennas at frequencies ranging from 10 to 90 GHz. It was revealed that at 30 GHz, the reconstruction errors for $psPD_{4cm2}$ were less than 0.8 dB and 0.2 dB on evaluation planes 2 and 5 mm, respectively, in front of the antennas. The robustness of the proposed method against the noise, scan range, and number of spherical modes were evaluated. The proposal may eliminate conventional compliance assessment procedures once antenna performance is evaluated in spherical near-field measurement.

INDEX TERMS Exposure assessment, spherical near-field measurement, standardization.

I. INTRODUCTION

The fifth-generation (5G) wireless communication adopts a frequency band of 26–28 GHz for high-speed data transfer. The new frequency assignment raises potential public concern about the possible heating effect of electromagnetic field (EMF) exposure. Recently, the IEEE International Committee on Electromagnetic Safety (ICES) and International Commission on Non-Ionizing Radiation Protection (ICNIRP) revised their standard and guidelines [1], [2]. For human exposure to EMF above 6 GHz, an absorbed power density (APD) was introduced as a basic restriction (named the dosimetry reference limit in the IEEE standard) to prevent excessive skin temperature rise for local exposure. Then, the (exposure) reference level was specified in terms of the spatial-average incident power density (IPD) in free space based on body transmittance and correlation with peak temperature rise [3]–[8].

Dosimetry studies have been conducted to evaluate the APD, spatial-average power density (*s*PD) in free space, and the resultant temperature rise in skin models [9]–[13]. The permissible output power levels of 5G devices above 6 GHz were also estimated [14], [15]. As many portable wireless devices are designed to be used near the human body, assessment methods for peak spatial-average power density (*ps*PD) above 6 GHz are needed to ensure the compliance of an actual device [16]. Currently, a standard assessment method for *ps*PD is under development by the International Electrotechnical Commission and IEEE ICES [17].

Several methods have been proposed for the *ps*PD assessment. The *ps*PD was assessed based on the planar near-field measurement, and the computation error was investigated using a method based on planar near-field transformation [18]. One drawback of this approach is that a large measurement plane is needed, particularly for a low- or

The associate editor coordinating the review of this manuscript and approving it for publication was Davide Ramaccia.

medium-directivity antenna and a directional antenna with a large scan angle. A pseudovector probe was adopted for the *ps*PD assessment [19], which can be reconstructed based on a measured field polarization ellipse. However, the retrieved phase from a polarization ellipse still represents a source of uncertainty that cannot be eliminated [20]. The coupling between an antenna and a probe also cannot be easily mitigated. An equivalent current method was proposed in [21], and a 1.1-dB error was found on an evaluation plane 5 mm in front of the antenna; however, a dense sampling was required for the reconstruction error to be below that level.

Spherical near-field measurement is a widely adopted antenna measurement technique [22]. The characteristics of an antenna can be extracted based on the spherical wave expansion (SWE) of sampled electric field (EF) or magnetic field (MF) components on a measurement sphere. Compared with planar near-field measurement, the spherical measurement is characterized by its full coverage of all potential radiation angles. Therefore, it would be advantageous if the *ps*PD can be directly assessed from the spherical near-field measurement data of the antenna. In our previous study [23], a hybrid SWE and finite-difference time-domain (FDTD) method was developed for APD assessment in an exposed human body model. However, one limitation was that the evaluation distance should be larger than the radius of the minimum enclosing sphere.

In this study, we adapted the SWE to plane wave expansion (PWE) technique, which allowed the backward transformation of the EMF from the measurement sphere to a plane just in front of the antenna aperture. The SWE-to-PWE transformation was originally developed for antenna array diagnosis [24]. Primary attention was paid to the EF distribution rather than the actual power densities. As the probe is usually placed at several wavelengths from the antenna to mitigate the coupling effect, one unresolved issue for this approach is the *ps*PD assessment accuracy, which requires information about both EF and MF phasors. In this study, we first developed an SWE-to-PWE transformation algorithm to reconstruct the EF and MF on an evaluation plane. The estimated *ps*PD accuracy from reconstructed fields was validated by considering 12 array antennas at frequencies ranging from 10 to 90 GHz. Moreover, the effects of measurement noise, number of samples, and scan range were numerically evaluated, thereby confirming the applicability of the proposed *ps*PD assessment method.

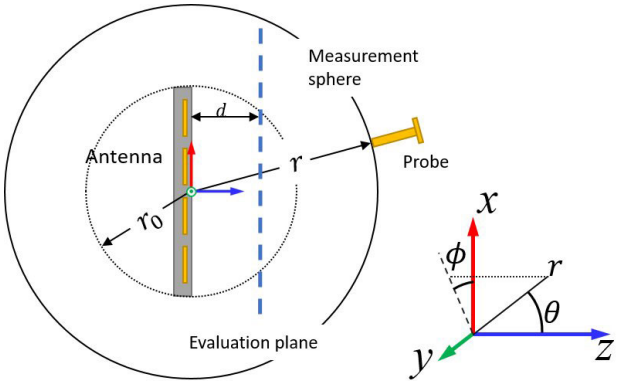

FIGURE 1. Schematic of the SWE-to-PWE method to assess *ps*PD on an evaluation plane at distance d from the array antenna aperture.

II. SWE-TO-PWE METHOD FOR psPD ASSESSMENT

Fig. 1 illustrates a schematic of the SWE-to-PWE method to assess the *ps*PD on an evaluation plane at a distance d from an antenna surface. The EF components of the antenna were sampled on a sphere as the measurement data. Using the spherical near-field transformation [25], the probe received signal, $w(r, \chi, \theta, \phi)$ can be expressed as follows:

$$w(r,\chi,\theta,\phi) = \sum_{\mu=\pm1}\sum_{s=1}^{2}\sum_{n=1}^{N}\sum_{m=-n}^{n} Q_{smn} \cdot e^{im\phi} d^{n}_{\mu m}(\theta)\, e^{i\mu\chi} P_{s\mu n}(kr), \quad (1)$$

where (r, θ, ϕ) is probe location in a spherical coordinate, χ, and $e^{im\phi} d^{n}_{\mu m}(\theta)\, e^{i\mu\chi}$ are rotation angle of the probe, and rotation coefficient of the spherical wave functions, respectively. The indices s, m, and n are limited to $s = 1, 2, m = -N, \ldots, 0, \ldots, N$, and $n = |m|, \ldots, N (n \neq 0)$, where N is the number of spherical modes and is commonly determined by $N = [kr_0] + 10$, with $[x]$ denoting the greatest integer no larger than x, and r_0 is the radius of the antenna minimum sphere. The mode numbers for different antennas for *ps*PD reconstruction are summarized in Table 1. If the probe received signal $w(r, \chi, \theta, \phi)$ is known, the complex amplitudes of the spherical waves Q_{smn} can be determined using Eq. (1). Then, the PWE of an EF, $\vec{T}(k_x, k_y)$, is obtained from Q_{smn} as follows [24]:

$$\vec{T}(k_x,k_y)\, e^{ik_z z} = \sum_{s=1}^{2}\sum_{n=1}^{N}\sum_{m=-n}^{n} Q_{smn}\vec{T}_{smn}(k_x,k_y,z), \quad (2)$$

where

$$\vec{T}_{1mn}(k_x,k_y,z) = \frac{e^{ik_z z}}{k_z}\frac{(-i)^{n+1}}{\sqrt{\eta}\sqrt{n(n+1)}}\vec{Y}^{m}_{n}(\alpha,\beta) \quad (3)$$

$$\vec{T}_{2mn}(k_x,k_y,z) = \frac{e^{ik_z z}}{k_z}\frac{(-i)^{n+1}\,\hat{k}}{\sqrt{\eta}\sqrt{n(n+1)}} \times \vec{Y}^{m}_{n}(\alpha,\beta) \quad (4)$$

The function $\vec{Y}^{m}_{n}$ is the vector spherical harmonics [24]. Similarly, the PWE of an MF can be obtained as follows:

$$\vec{T}^{H}(k_x,k_y) = (\epsilon/\mu)^{1/2}\,\hat{k} \times \vec{T}(k_x,k_y) \quad (5)$$

Knowing both the electric and magnetic plane wave spectra, the EF and MF on plane $z = d$ are expressed by Eqs. (6) and (6) and can be numerically obtained by the fast Fourier transform.

$$\vec{E}(x,y,d) = \frac{1}{2\pi}\iint_{-\infty}^{+\infty}\vec{T}(k_x,k_y)\, e^{i(k_x x + k_y y + k_z d)}dk_x dk_y \quad (6)$$

$$\vec{H}(x,y,d) = \frac{1}{2\pi}\iint_{-\infty}^{+\infty} \vec{T}^H(k_x,k_y)\, e^{i(k_x x+k_y y+k_z d)} dk_x dk_y \tag{7}$$

Then, the *s*PD can be obtained based on the time-average Poynting vector:

$$s\text{PD} = \frac{1}{2A}\iint_A \left\| \text{Re}\left[\vec{E}\times\vec{H}^*\right]\right\| dA, \tag{8}$$

where A is the averaging area. The *s*PD is averaged over a square area of 4 cm^2. For frequencies ≥30 GHz, an additional criterion that the *s*PD should be averaged over 1 cm^2 for narrow beam applies [2]. Both averaging areas were considered in this study.

III. SIMULATION MODELS

Twelve array antennas were considered for the SWE-to-PWE transformation-based method validation. Table 1 summarizes the antenna types and configurations adopted in this study. Five operation frequencies, 10, 15, 30, 60, and 90 GHz, were considered. The geometric parameters for a 4 × 4 dipole array and 3 × 3 patch array antennas are illustrated in Fig. 2 as examples. Note that the dipole arrays are idealized antenna, which were used as test models for validating the applicability of the proposed approach. Patch antennas were backed by a large ground plane. The substrate relative permittivity was 2.2, with a thickness t. To obtain the space EF and MF around the antenna, in-house FDTD [26] code, which had been validated previously [10], [27], was employed. Simulations were performed at 30 GHz using a spatial resolution of 0.25 mm to satisfy the Courant condition. A 10-layer convolutional perfectly matched layer [28] was used to truncate the simulation domains. The antennas were placed in the center of the simulation domains. Array elements were excited by a delta-gap voltage source in FDTD with equal amplitudes and phases. Thus, the main beams of adopted array antennas point at the z-direction (Fig. 1). Results for other frequencies were scaled from the simulation results obtained at 30 GHz. The antenna geometric parameters after frequency scaling are summarized in Table 2.

TABLE 1. Configuration of array antennas.

Antenna	Configuration	Number of Modes
Dipole array	2 × 2	14
Dipole array	4 × 1	15
Dipole array	4 × 2	16
Dipole array	4 × 4	18
Dipole array	8 × 2	21
Dipole array	8 × 4	23
Dipole array	8 × 8	27
Patch array	2 × 2	46
Patch array	3 × 3	46
Patch array	4 × 1	46
Patch array	4 × 2	46
Patch array	4 × 4	46

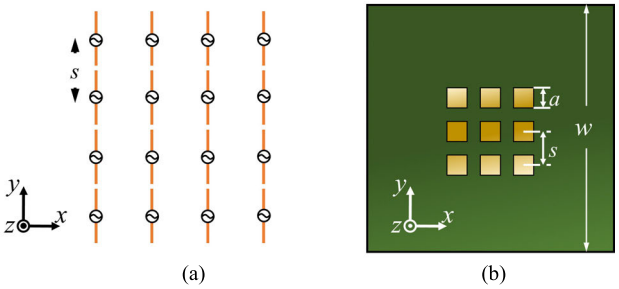

(a) (b)

FIGURE 2. Geometric parameters of (a) dipole array and (b) patch array at 30 GHz.

TABLE 2. Antenna geometric parameters.

Frequency [GHz]	a [mm]	s [mm]	t [mm]	w [mm]
10	9	15	1.5	120
15	6	10	1	80
30	3	5	0.5	40
60	1.5	2.5	0.25	20
90	1	1.67	0.167	13.3

The EF components E_θ and E_ϕ in spherical coordinates were sampled on a sphere with a radius of 5 λ to simulate the input measurement data for the SWE-to-PWE transformation. The sampling resolution was determined by $\Delta\theta = \Delta\phi \leq 360°/(2N+1)$. Then, free-space IPDs were reconstructed on three evaluation planes at $d = 2$, 5, and 10 mm in front of the antenna aperture. A resolution of 0.5 mm was used on each evaluation plane to obtain the IPD and perform the spatial averaging. Then, the *ps*PDs averaged over 4 and 1 cm^2 were evaluated using Eq. (8). For validation of the proposed SWE-to-PWE transformation-based method, we compared the reconstructed IPD to those obtained directly from the FDTD simulations.

IV. RESULTS

A. POWER DENSITY DISTRIBUTIONS

Figs. 3 and 4, respectively, show the reconstructed free-space IPD distributions for the 4 × 4 dipole array and 3 × 3 patch array antennas at 30 GHz on different evaluation planes. The size of the observation plane was set to 10 × 10 cm^2. The reconstructed IPD distributions resemble those obtained from full-wave simulations. Slight differences were observed on the evaluation plane of 2 mm from the antenna aperture, mainly attributable to the negligence of evanescent waves in the backward transformation. For $d = 5$ and 10 mm, the reconstructed IPD distributions within the main beams agreed well with the simulated IPD, with small ripples observed around the observation plane borders. From Figs. 3 and 4, the ripple levels were well below −20 dB of the peak value.

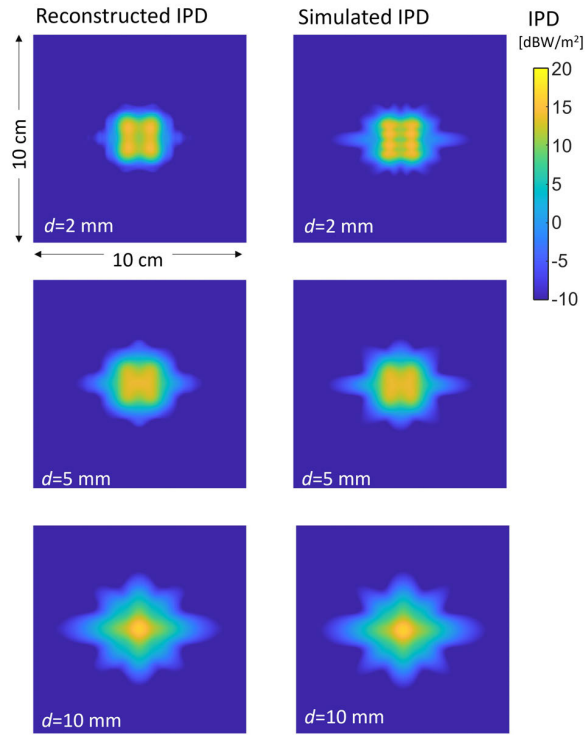

FIGURE 3. Reconstructed IPD distributions for 4 × 4 dipole array at 30 GHz on evaluation planes in front of the antenna. The antenna accepted power was normalized to 10 mW.

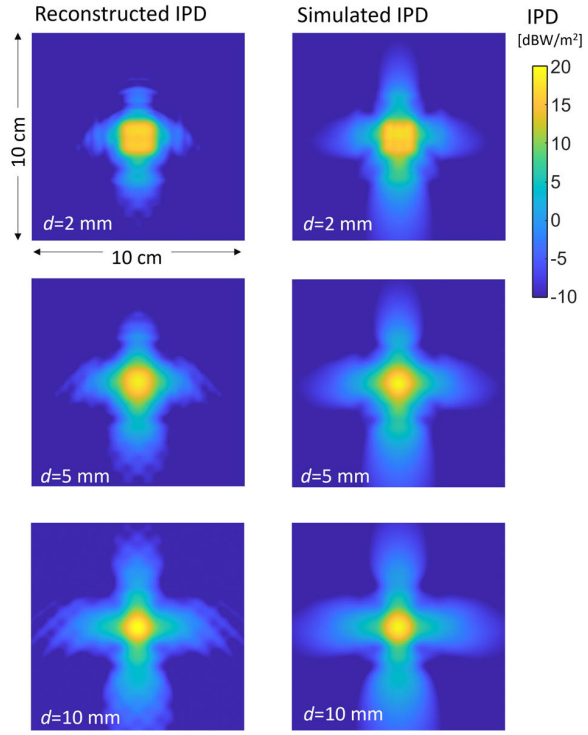

FIGURE 4. Reconstructed IPD distributions for 3 × 3 patch array at 30 GHz on evaluation planes in front of the antenna. The antenna accepted power was normalized to 10 mW.

B. PEAK SPATIAL-AVERAGE POWER DENSITY

We compared the reconstructed *ps*PD with those obtained from the FDTD full-wave simulations. The boxplots for the relative differences (RDs) between the reconstructed and simulated $psPD_{4cm2}$ are shown in Fig. 5. The largest RD was ~ -2 dB at the evaluation plane of 2 mm and lowest considered frequency 10 GHz. The averages and interquartile ranges of RDs drastically decreased with an increase in frequency. At 30 GHz, which is close to the frequency band allocated for the 5G communication, the largest and average RDs from the simulation results were -0.8 and -0.25 dB, respectively, at $d = 2$ mm. The increasing distance between the antenna and evaluation plane decreased the RDs. At $d = 10$ mm, the largest RD in $psPD_{1cm2}$ was $\sim$0.4 dB at 10 GHz and decreased to $\sim$0.1 dB at frequencies $\geq$30 GHz. The RDs in $psPD_{1cm2}$ are shown in Fig. 6 for frequencies $\geq$30 GHz. The tendencies were similar to those for $psPD_{4cm2}$.

C. EFFECT OF MEASUREMENT NOISE

We studied the effect of the additive noise to the amplitude and phase on the reconstructed *ps*PD. For phase noise, the white Gaussian noises with standard deviations (SDs) of 2°, 5°, 10°, and 20° were added to the real phases for the 4 × 4 dipole array. For amplitude noise, we considered three levels of white Gaussian noises from -40 to -20 dB. The amplitude noise levels were set relative to the maximum sampled power on the measurement sphere. For each noise level combination, 300 simulations were performed for a Monte Carlo analysis of the effect of measurement noise. Fig. 7 shows the IPD distributions for different combinations of measurement noises. Increased ripple levels were observed for high measurement noises. In Fig. 8(a), the average and SD of the RDs in the $psPD_{4cm2}$ ($d = 2$ mm) increased from (0.032 ± 0.0052) dB (average ± SD) to (0.51 ± 0.053) dB when the phase noise SD increased from 2° to 20° (with no amplitude noise). Increasing phase noise widened the RD interquartile ranges and decreased the *ps*PD values compared with the results without phase noise.

From Figs. 8(b)–(d), the amplitude noises with levels from -40 to -20 dB were considered together with the phase noises. Increasing the amplitude noise widened the RD interquartile ranges. The RD interquartile ranges of RDs caused by the amplitude noise level of -30 and -20 dB only (without phase noises) were $\sim\pm0.2$ and ±0.5 dB, respectively. From the results, it is recommended that the noise levels in amplitude and phase were below -30 dB and 10°, respectively.

D. EFFECT OF NUMBER OF SPHERICAL MODES

The effects of the number of spherical modes on the accuracy of reconstructed *ps*PD were also evaluated. The antenna considered here was the 4 × 4 dipole array at 30 GHz. The evaluation plane was 2 mm in front of the antenna. The mode number was increased from $[kr_0]+10$ to $[kr_0]+60$ at an interval of 10, for the SWE-to-PWE transformation. The results are summarized in Table 3. The reconstructed $psPD_{4cm2}$ and $psPD_{1cm2}$ were almost unaffected by the mode number when $N \geq [kr_0]+10$. In addition, the results agreed well with those

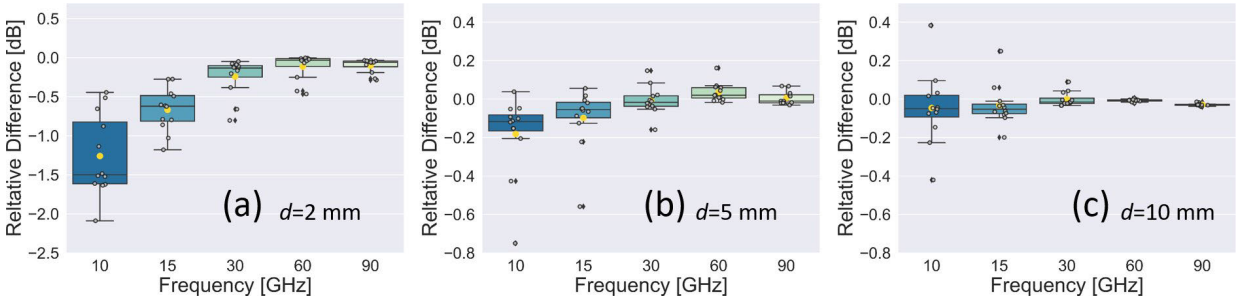

FIGURE 5. RD of the reconstructed psPD averaged over 4 cm^2 for (a) $d = 2$ mm, (b) $d = 5$ mm, and (c) $d = 10$ mm. The box indicates the range from the first quartile to the third quartile. The black line in middle of the box represents the median. The yellow circle represents the average value. The whiskers indicate the smallest and largest non-outlier values.

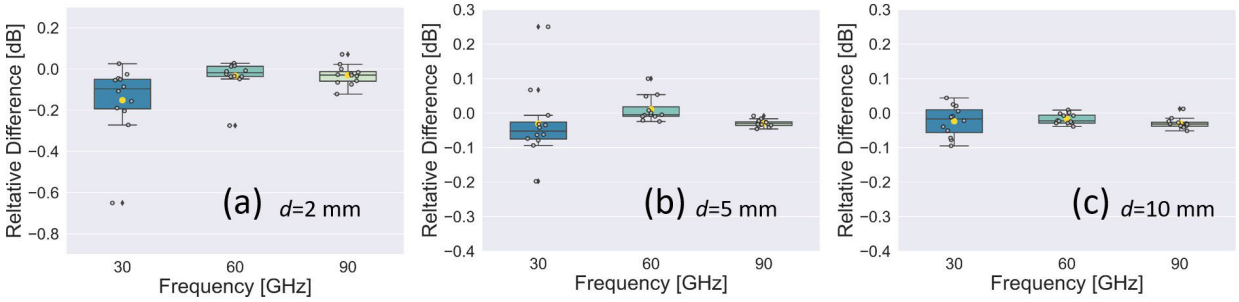

FIGURE 6. RD of the reconstructed psPD averaged over 1 cm^2 for (a) $d = 2$ mm, (b) $d = 5$ mm, and (c) $d = 10$ mm. The box indicates the range from the first quartile to the third quartile. The black line in middle of the box represents the median. The yellow circle represents the average value. The whiskers indicate the smallest and largest non-outlier values.

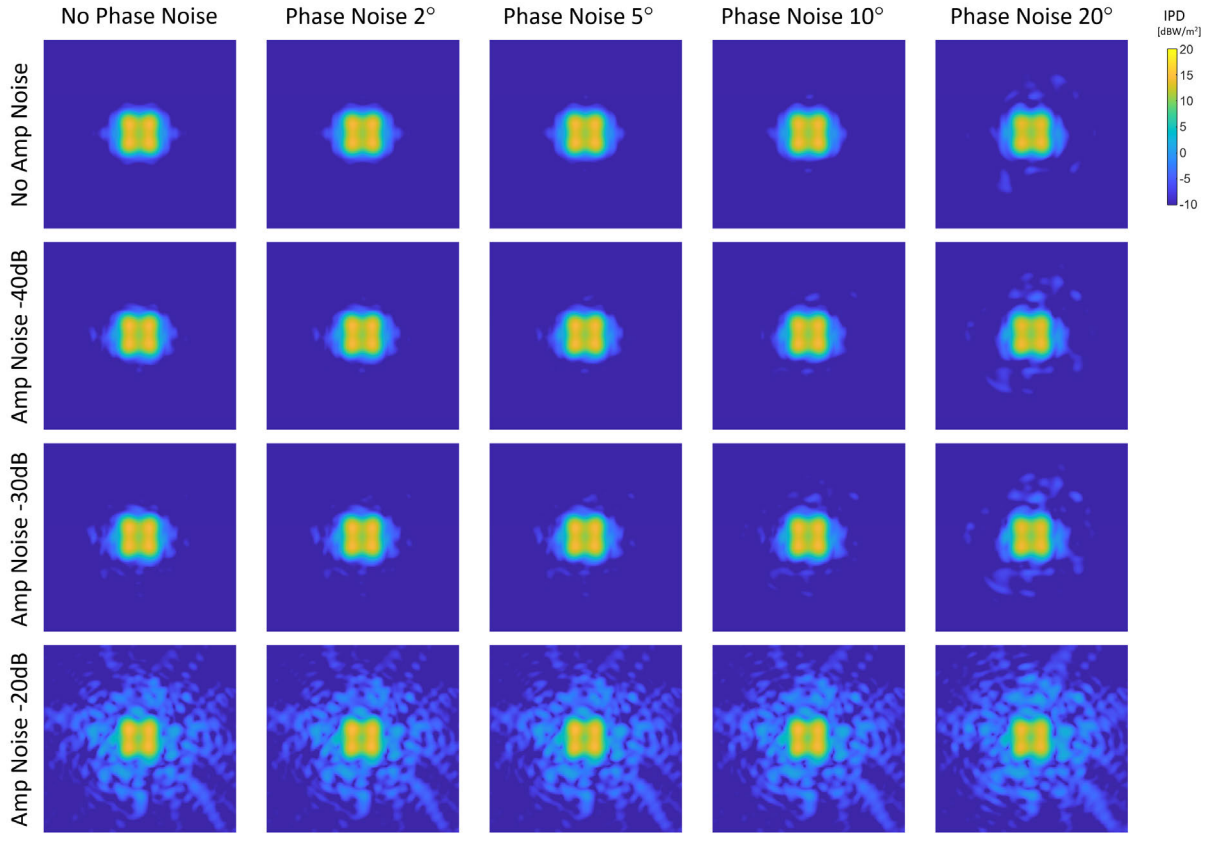

FIGURE 7. Reconstructed IPD with different levels of noises in amplitudes and phases of the measurement samples. The antenna accepted power was normalized to 10 mW.

computed using FDTD simulations, $psPD_{4cm2} = 12.206$ and $psPD_{1cm2} = 12.922$ dBW/m^2.

E. EFFECT OF SCAN RANGE

Fig. 9 shows the effect of scan range in θ (shown in Fig. 1) on the reconstructed *ps*PD. The frequency was set to 30 GHz and $d = 2$ mm. All 12 antennas were considered. The scan range in θ increased from $\pm 30°$ to $\pm 120°$. For a $\pm 30°$ scan range, the maximum deviation from the simulated *ps*PD was ~5 dB, the highest RD was found for the array antennas

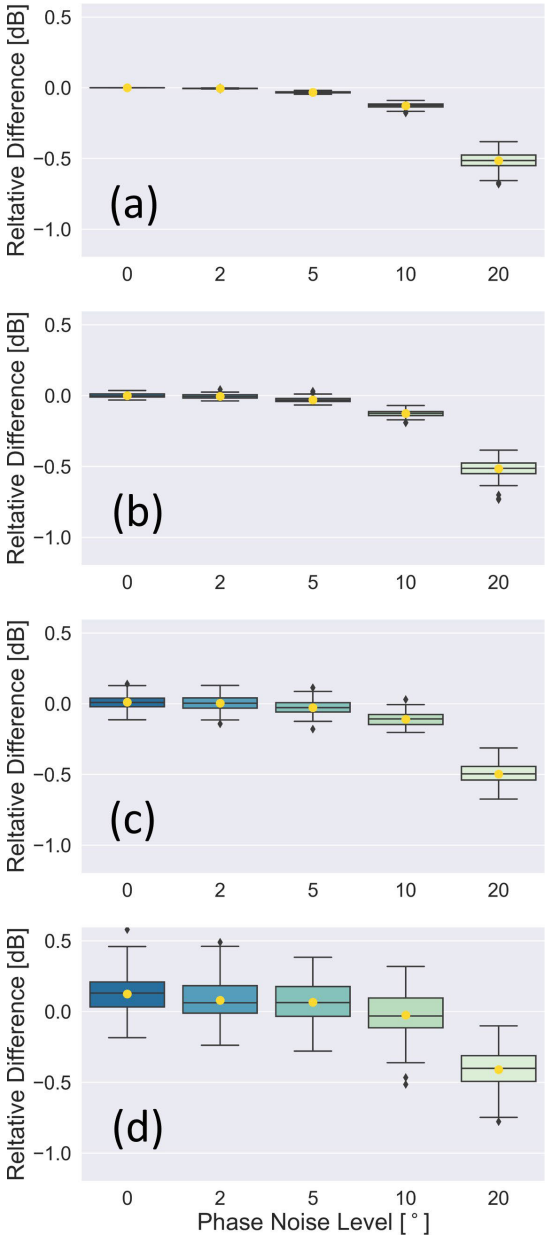

FIGURE 8. RDs caused by the additive noise of the sampled electric fields on measurement sphere. (a) No amplitude noise, (b) −40 dB amplitude noise, (c) −30 dB amplitude noise, and (d) −20 dB amplitude noise. The box indicates the range from the first quartile to the third quartile. The black line in middle of the box represents the median. The yellow circle represents the average value. The whiskers indicate the smallest and largest non-outlier values.

TABLE 3. Dependence of *ps*PD on number of spherical modes.

Number of Modes	$psPD_{1cm2}$ [dBW/m^2]	$psPD_{4cm2}$ [dBW/m^2]
$N = [kr_0] + 10$	12.9479	12.1000
$N = [kr_0] + 20$	12.9588	12.1046
$N = [kr_0] + 30$	12.9550	12.1032
$N = [kr_0] + 40$	12.9574	12.1048
$N = [kr_0] + 50$	12.9539	12.1026
$N = [kr_0] + 60$	12.9512	12.0990

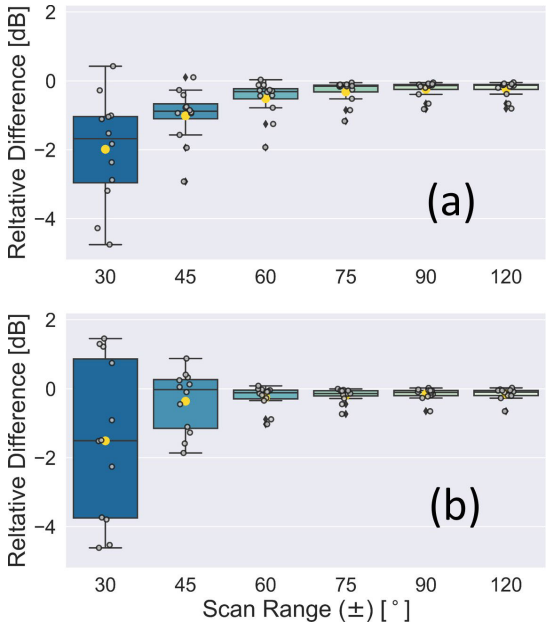

FIGURE 9. RDs in (a) $psPD_{4cm2}$ and (b) $psPD_{1cm2}$ caused by the scan range. The box indicates the range from the first quartile to the third quartile. The black line in middle of the box represents the median. The yellow circle represents the average value. The whiskers indicate the smallest and largest non-outlier values.

with relatively low directivities as expected. For scan ranges of $\pm 30°$ and $\pm 45°$, the RD interquartile ranges in $psPD_{1cm2}$ were larger than those in $psPD_{4cm2}$. For scan ranges not less than $\pm 75°$, the RDs were almost identical to those obtained from a full spherical scan for both $psPD_{4cm2}$ and $psPD_{1cm2}$ for the antennas adopted.

V. DISCUSSION AND CONCLUDING REMARKS

The spherical near-field measurement is a widely adopted antenna measurement technique. Therefore, the compliance assessment using the spherical near-field measurement data would be desirable, as efforts for additional assessment can be saved. In this study, we first developed an algorithm for assessing *ps*PD using the SWE-to-PWE transformation-based method. This proposal may potentially formulate an effective compliance assessment method that can eliminate the procedure of additional measurement once the antenna performance is evaluated by the spherical

near-field measurement. This approach is particularly useful for evaluating new wireless communication applications, such as 5G devices.

For the reconstruction method based on planar near-field measurement, a large measurement area is needed, particularly for low- or medium-directivity antennas, to suppress the truncation error. Meanwhile, the method based on spherical measurement can cover all potential radiation directions with the same number of measurement samples. Since phased array antennas with high directivity will more likely be used in the mmWave bands for 5G communication, the spherical measurement samples can be further reduced (Subsection IV-E). In addition, the probe always points at the antenna during a spherical scan. By contrast, in the planar near-field measurement, the probe is not pointed at the antenna at all times, and the probe–antenna distance varies during the planar scan, which subsequently restricts the largest scan area that can be employed.

In [24], the number of spherical modes was selected to be larger than that usually adopted in spherical near-field antenna measurement systems. The purpose was to obtain a more localized EF distribution on the antenna aperture. This is reasonable for antenna diagnosis. A large mode number mainly influences the invisible region of PWE [18], which corresponds to the exponentially attenuated evanescent waves that cannot be accurately determined for a measurement distance of several wavelengths. Including more waves in the invisible region may also lead to singularities when performing the back transformation [24], as seen from the results; the common choice of mode number ($N = [kr_0]+10$) can exhibit converged *ps*PD results. The effect of measurement noise was investigated. It was recommended that the noise levels of amplitude and phase should be lower than -30 dB and $10°$, respectively, to suppress the reconstruction errors caused by noises. The abovementioned general criterion for restricting measurement noise agrees with those reported in [18], [21], although different approaches were used.

From Figs. 5 and 6, the largest RDs always appeared on the evaluation plane at $d = 2$ mm. Except for this very close exposure scenario, the RDs in reconstructed *ps*PDs were small for $d = 5$ and 10 mm. From Fig. 5(b), the RDs are within ± 0.2 dB for all antennas for $d = 5$ mm at 30 GHz, indicating good accuracy of the SWE-to-PWE method for assessing *ps*PD. In the ICNIRP guidelines [2], it was mentioned that compliance can be demonstrated using *ps*PD within the far-field and radiative near-field zones, whereas assessment using APD is needed in the reactive near-field zone. As a rough guide, the guidelines [2] suggested $< \lambda/2\pi$ as the reactive near-field region and mentioned that "*it is anticipated that input from technical standards bodies should be used to better determine which of the far-field/near-field zone reference level rules should be applied to provide appropriate concordance between reference levels and basic restrictions*" [2]. In standard IEC 62232-2017, the reactive near-field boundary for linear or planar antenna arrays (with a maximum dimension of $\geq 2.5\lambda$) was specified as λ (Table A.4) [29]. Considering the abovementioned implications of field zones, the evaluation plane at $d = 2$ mm may locate in the reactive near-field zone for the array antennas adopted in this study. If these extremely close exposure cases are excluded, better accuracy in reconstructed *ps*PD can be expected for the SWE-to-PWE transformation-based method.

In summary, a SWE-to-PWE transformation-based method was proposed for the *ps*PD assessment for mmWave antennas. Good agreement between the reconstructed *ps*PDs and simulation results were observed. The robustnesses against noise, scan range, and mode number were evaluated. The results showed that the proposed method can be applied for a fast *ps*PD assessment for 5G mmWave devices. Future study may investigate the large-beam-angle scenarios for phased array antennas and simultaneous exposures from multiple sources.

REFERENCES

[1] *IEEE Standard for Safety Levels With Respect to Human Exposure to Electric, Magnetic and Electromagnetic Fields, 0 kHz to 300 GHz*, Standard IEEE C95.1, New York, NY, USA, 2019.

[2] International Commission on Non-Ionizing Radiation Protection, "Guidelines for limiting exposure to electromagnetic fields (100 kHz to 300 GHz)," *Health Phys.*, vol. 118, no. 5, pp. 483–524, 2020, doi: 10.1097/hp.0000000000001210.

[3] K. R. Foster, M. C. Ziskin, and Q. Balzano, "Thermal response of human skin to microwave energy: A critical review," *Health Phys.*, vol. 111, no. 6, 2016, doi: 10.1097/HP.0000000000000571.

[4] Y. Hashimoto, A. Hirata, R. Morimoto, S. Aonuma, I. Laakso, K. Jokela, and K. R. Foster, "On the averaging area for incident power density for human exposure limits at frequencies over 6 GHz," *Phys. Med. Biol.*, vol. 62, pp. 3124–3138, 2017.

[5] K. Sasaki, M. Mizuno, and K. Wake, "Monte Carlo simulations of skin exposure to electromagnetic field from 10 GHz to 1 THz," *Phys. Med. Biol.*, vol. 62, no. 17, pp. 6993–7010, 2017.

[6] A. Hirata, S. Kodera, K. Sasaki, J. Gomez-Tames, I. Laakso, A. Wood, S. Watanabe, and K. R. Foster, "Human exposure to radiofrequency energy above 6 GHz: Review of computational dosimetry studies," *Phys. Med. Biol.*, vol. 66, no. 8, Apr. 2021, Art. no. 08TR01, doi: 10.1088/1361-6560/abf1b7.

[7] K. Li, K. Sasaki, S. Watanabe, and H. Shirai, "Relationship between power density and surface temperature elevation for human skin exposure to electromagnetic waves with oblique incidence angle from 6 GHz to 1 THz," *Phys. Med. Biol.*, vol. 64, no. 6, Mar. 2019, Art. no. 065016, doi: 10.1088/1361-6560/ab057a.

[8] D. Funahashi, A. Hirata, S. Kodera, and K. R. Foster, "Area-averaged transmitted power density at skin surface as metric to estimate surface temperature elevation," *IEEE Access*, vol. 6, pp. 77665–77674, 2018, doi: 10.1109/ACCESS.2018.2883733.

[9] T. Nakae, D. Funahashi, J. Higashiyama, T. Onishi, and A. Hirata, "Skin temperature elevation for incident power densities from dipole arrays at 28 GHz," *IEEE Access*, vol. 8, pp. 26863–26871, 2020, doi: 10.1109/ACCESS.2020.2970219.

[10] Y. Diao, E. A. Rashed, and A. Hirata, "Assessment of absorbed power density and temperature rise for nonplanar body model under electromagnetic exposure above 6 GHz," *Phys. Med. Biol.*, vol. 65, no. 22, 2020, Art. no. 224001, doi: 10.1088/1361-6560/abbdb7.

[11] E. Carrasco, D. Colombi, K. R. Foster, M. Ziskin, and Q. Balzano, "Exposure assessment of portable wireless devices above 6 GHz," *Radiat. Protection Dosimetry*, vol. 183, no. 4, pp. 489–496, 2019, doi: 10.1093/rpd/ncy177.

[12] M. S. Morelli, S. Gallucci, B. Siervo, and V. Hartwig, "Numerical analysis of electromagnetic field exposure from 5G mobile communications at 28 GHZ in adults and children users for real-world exposure scenarios," *Int. J. Environ. Res. Public Health*, vol. 18, no. 3, p. 1073, Jan. 2021, doi: 10.3390/ijerph18031073.

[13] D. Poljak and M. Cvetković, "Assessment of absorbed power density (S_{ab}) at the surface of flat lossy medium in GHz frequency range : A case of Hertz dipole," in *Proc. 5th Int. Conf. Smart Sustain. Technol. (SpliTech)*, Sep. 2020, pp. 1–4, doi: 10.23919/SpliTech49282.2020.9243751.
[14] D. Colombi, B. Thors, and C. Törnevik, "Implications of EMF exposure limits on output power levels for 5G devices above 6 GHz," *IEEE Antennas Wireless Propag. Lett.*, vol. 14, pp. 1247–1249, 2015, doi: 10.1109/LAWP.2015.2400331.
[15] B. Thors, D. Colombi, Z. Ying, T. Bolin, and C. Törnevik, "Exposure to RF EMF from array antennas in 5G mobile communication equipment," *IEEE Access*, vol. 4, pp. 7469–7478, 2016, doi: 10.1109/ACCESS.2016.2601145.
[16] B. Xu, K. Zhao, B. Thors, D. Colombi, O. Lundberg, Z. Ying, and S. He, "Power density measurements at 15 GHz for RF EMF compliance assessments of 5G user equipment," *IEEE Trans. Antennas Propag.*, vol. 65, no. 12, pp. 6584–6595, Dec. 2017, doi: 10.1109/TAP.2017.2712792.
[17] *IEC/IEEE International Draft Standard—Assessment of Power Density of Human Exposure to Radio Frequency Fields From Wireless Devices in Close Proximity to the Head and Body—Part 2: Computational Procedure (Frequency Range of 6 GHz to 300 GHz)*, Standard IEEE/IEC P63195-2, 2019.
[18] K. Sasaki, K. Li, J. Chakarothai, T. Iyama, T. Onishi, and S. Watanabe, "Error analysis of a near-field reconstruction technique based on plane wave spectrum expansion for power density assessment above 6 GHz," *IEEE Access*, vol. 7, pp. 11591–11598, 2019, doi: 10.1109/ACCESS.2019.2891939.
[19] S. Pfeifer, E. Carrasco, P. Crespo-Valero, E. Neufeld, S. Kühn, T. Samaras, A. Christ, M. H. Capstick, and N. Kuster, "Total field reconstruction in the near field using pseudo-vector E-field measurements," *IEEE Trans. Electromagn. Compat.*, vol. 61, no. 2, pp. 476–486, Apr. 2019, doi: 10.1109/TEMC.2018.2837897.
[20] J. Lundgren, J. Helander, M. Gustafsson, D. Sjoberg, B. Xu, and D. Colombi, "A near-field measurement and calibration technique: Radio-frequency electromagnetic field exposure assessment of millimeter-wave 5G devices," *IEEE Antennas Propag. Mag.*, vol. 63, no. 3, pp. 77–88, Jun. 2021, doi: 10.1109/MAP.2020.2988517.
[21] W. He, B. Xu, L. Scialacqua, Z. Ying, A. Scannavini, L. J. Foged, K. Zhao, C. Di Paola, S. Zhang, and S. He, "Fast power density assessment of 5G mobile handset using equivalent currents method," *IEEE Trans. Antennas Propag.*, early access, Apr. 8, 2021, doi: 10.1109/TAP.2021.3070725.
[22] O. Breinbjerg, "Spherical near-field antenna measurements—The most accurate antenna measurement technique," in *Proc. IEEE Int. Symp. Antennas Propag. (APSURSI)*, Jun. 2016, pp. 1019–1020, doi: 10.1109/APS.2016.7696217.
[23] Y. Diao and A. Hirata, "Exposure assessment of array antennas at 28 GHz using hybrid spherical near-field transformation and FDTD method," *IEEE Trans. Electromagn. Compat.*, early access, May 17, 2021, doi: 10.1109/TEMC.2021.3074658.
[24] C. Cappellin, O. Breinbjerg, and A. Frandsen, "Properties of the transformation from the spherical wave expansion to the plane wave expansion," *Radio Sci.*, vol. 43, no. 1, Feb. 2008, Art. no. RS1012, doi: 10.1029/2007rs003696.
[25] J. E. Hansen, *Spherical Near-field Antenna Measurements*. London, U.K.: Peter Peregrinus, 1988.
[26] A. Taflove and S. C. Hagness, *Computational Electrodynamics: The Finite-Difference Time-Domain Method*, 3rd ed. Norwood, MA, USA: Artech House, 2005.
[27] Y. Diao, E. A. Rashed, and A. Hirata, "Large-scale analysis of the head proximity effects on antenna performance using machine learning based models," *IEEE Access*, vol. 8, pp. 154060–154071, 2020, doi: 10.1109/ACCESS.2020.3017773.
[28] J. A. Roden and S. D. Gedney, "Convolutional PML (CPML): An efficient FDTD implementation of the CFS-PML for arbitrary media," *Microw. Opt. Technol. Lett.*, vol. 27, no. 5, pp. 334–338, 2000.
[29] *Determination of RF Field Strength, Power Density and SAR in the Vicinity of Radiocommunication Base Stations for the Purpose of Evaluating*, Standard IEC 62232:2017, 2017.

YINLIANG DIAO (Member, IEEE) received the B.E. degree in electronic information engineering from Chongqing University, Chongqing, China, in 2008, the M.S. degree in electronic engineering from Beijing University of Posts and Telecommunications, Beijing, China, in 2011, and the Ph.D. degree in electronic engineering from the City University of Hong Kong, in 2016. Since 2017, he has been an Assistant Professor with South China Agricultural University, Guangzhou, China. In 2019, he joined the Department of Electrical and Mechanical Engineering, Nagoya Institute of Technology, where he is currently a Research Associate Professor. His current research interests include electromagnetic dosimetry modeling and electromagnetic compatibility. He is a member of the IEEE ICES Standards Coordinating Committee and the Scientific Expert Group of International Commission on Non-Ionizing Radiation Protection. He was a recipient of the Young Scientist Award from URSI GASS 2020.

AKIMASA HIRATA (Fellow, IEEE) received the B.E., M.E., and Ph.D. degrees in communications engineering from Osaka University, Suita, Japan, in 1996, 1998, and 2000, respectively.

He was a Visiting Research Scientist with the University of Victoria, Victoria, BC, Canada, in 2000. In 2001, he joined the Department of Communications Engineering, Osaka University, as an Assistant Professor. In 2004, he joined as an Associate Professor with the Department of Computer Science and Engineering, Nagoya Institute of Technology, where he is currently a Full Professor. His research interests include electromagnetic safety, risk management system for heat-related illness, methods in neuroscience, antennas, filters, and related computational techniques.

Prof. Hirata is a fellow of the Institute of Physics and a member of IEICE, IEE Japan, and the Bioelectromagnetics Society. From 1999 to 2001, he was a Research Fellow of Japan Society for the Promotion of Science. He received several awards, including the Young Scientists' Prize, in 2006, and the Prizes for Science and Technology, such as Research Category 2011 and Public Understanding Promotion Category 2014 and 2020) by the Commendation for Science and Technology by the Ministry of Education, Culture, Sports, Science, and Technology, Japan, the IEEE EMC-S Technical Achievement Award, in 2015, and Japan Academy Medal and JSPS Prize, in 2018. He is a member of the main commission and the Chair of the Project Group of the International Commission on Non-Ionizing Radiation Protection, and a member of the Administrative Committee and the Subcommittee (EMF Dosimetry Modeling) Chair of the IEEE International Committee on Electromagnetic Safety, and an Expert of World Health Organization. From 2006 to 2012, he was an Associate Editor of the IEEE TRANSACTIONS ON BIOMEDICAL ENGINEERING. He is an Editorial Board Member of *Physics in Medicine and Biology*.